Nonlinear Dyn
https://doi.org/10.1007/s11071-025-11232-x

RESEARCH

Stability boundaries and bifurcation analysis of an AWD vehicle: the influence of the drive torque distribution

Manuel Eberhart · Manfred Plöchl · Johannes Edelmann

Received: 5 February 2025 / Accepted: 8 April 2025

Abstract All-wheel drive electric vehicles, equipped with independent motors at the front axle and the rear axle, allow for adaptive drive torque distribution between the axles to influence handling and stability characteristics. To analyse manoeuvres at combined longitudinal and lateral accelerations, a quasi-steady-state assumption is used to apply bifurcation and continuation techniques. Different types of loss of stability are found and analysed. The Takens–Bogdanov bifurcation is studied in more detail, and it is shown that the respective branch represents the boundary between final understeer and final oversteer, and defines the stable envelope in the GG diagram. The drive torque distribution at the Takens–Bogdanov branch is therefore considered a good design criterion for a safe and performant powertrain control. Besides the Takens–Bogdanov branch, related Hopf and Fold branches are identified that define limits for practically reasonable drive torque distributions.

Keywords Vehicle handling · Vehicle dynamics · All-wheel drive · Stability · Bifurcation analysis · Drive torque distribution · Takens–Bogdanov bifurcation

M. Eberhart (✉) · M. Plöchl · J. Edelmann
Institute of Mechanics and Mechatronics, TU Wien, Getreidemarkt 9, 1060 Vienna, Austria
e-mail: manuel.eberhart@tuwien.ac.at

1 Introduction

Powertrains of electric vehicles are often equipped with more than one electric motor. Since the individual motors are not mechanically coupled and very responsive, they offer new possibilities for vehicle control systems. Considering the mutual influence of longitudinal and lateral tyre forces, the drive torques may improve the responsiveness and stability properties of the vehicle. However, for this purpose, a profound understanding of the impact of the drive torque distribution on the stability and handling properties of the vehicle is required to ensure effective and safe operation. The focus of this paper is to gain a better understanding of the influence of the front-to-rear drive torque distribution of an all-wheel drive (AWD) vehicle with two independent motors, one at the front axle and one at the rear axle, on its stability properties and quasi-steady-state handling performance. Therefore, the handling regime at combined longitudinal and lateral acceleration of the vehicle is considered, where the impact of longitudinal tyre forces on lateral tyre forces and consequently the front-to-rear drive torque distribution may modify handling and stability characteristics considerably.

The (quasi-)steady-state handling characteristics of vehicles are fundamentally important to assess its (open loop) stability properties and to judge the vehicle's response to driver steering commands, [1–3]. Depending on the longitudinal acceleration, both in driving and braking conditions, and the powertrain and control architecture, the handling characteristics and stability properties of the vehicle can significantly change, [4–6].

In [4], Klomp et al. analyse the impact of all-wheel drive (AWD), front-wheel drive (FWD) and rear-wheel drive (RWD) powertrain architectures on the handling characteristics and lateral acceleration potential of a vehicle. For this purpose, a method is proposed to determine an 'optimal' drive torque distribution using a quasi-steady-state description of the vehicle model.

Bucchi et al. [7] and Lenzo et al. [8] compare FWD and RWD vehicles with a focus on handling and yaw torque analysis. It is shown that an FWD powertrain is less prone to understeer in steady-state cornering due to the additional yaw torque of the longitudinal forces at the front axle.

Using a basic two degrees of freedom (DOF) vehicle model and a simplified Pacejka 'Magic Formula' tyre model, Ono et al. [9] show that vehicle loss of stability is caused by a saddle-node bifurcation (also denoted Fold bifurcation), which depends considerably on the rear lateral tyre force saturation. A steering control strategy is proposed to stabilise the motion of the vehicle.

A study on vehicle dynamics and stability, taking into account different friction potentials of the tyres at the front axle and the rear axle, is presented by Shen et al. in [10]. The joint point locus approach is applied to identify system equilibrium points and to assess their stability characteristics.

A fundamental study on a two DOF vehicle model is done by Della Rossa et al. in [11]. Various types of loss of stability for different combinations of effective tyre force characteristics at the front axle and the rear axle of the vehicle model are studied and discussed with the help of bifurcation analysis and the phase-plane diagram.

The impact of the effective tyre force characteristics on the stability behaviour of a vehicle are studied by Pauwelussen in [12], focusing on the appearance of limit cycles, whereas Farroni et al. investigate its influence on the handling diagram and on the phase-plane diagram in [13].

Horiuchi et al. [5] use a quasi-steady-state description to model a vehicle in combined lateral and longitudinal acceleration conditions. Using the steering angle as the bifurcation parameter, a Fold bifurcation is found for a vehicle under negative longitudinal acceleration and a fixed brake torque distribution.

Wang et al. analyse the stability properties of a vehicle at combined braking and steering in [14]. The stability of the vehicle is analysed for different speeds, steering angles and brake torques with the help of bifurcation analysis, equivalent equilibrium description and phase-plane analysis for an ideal constant brake distribution between the front axle and the rear axle.

In contrast to conventional brake systems, regenerative braking using electric motors allows for a variable brake force distribution between the front axle and the rear axle and may allow to extend the combined stable longitudinal and lateral acceleration envelope in the GG diagram.

Besides improving the stable handling envelope, in certain conventional and critical driving conditions, the control of the drive torque distribution may be beneficial to enhance the responsiveness of the vehicle. A 'responsiveness and stability metric' is used by Zang et al. [15] to control the front-to-rear drive torque distribution for improved responsiveness and stability properties of the vehicle.

To study the properties of the lateral motion of the vehicle during longitudinal acceleration, the quasi-steady-state assumption (equivalent equilibrium) is applied to convert the transient condition into a mechanical equivalent steady-state. This transformation allows for the use of mathematical methods used for linear systems. Horiuchi et al. consider the front-to-rear load transfer and longitudinal tyre forces in [5] by adding a virtual external force to the equation of motion of the vehicle in the longitudinal direction. Abe applies a quasi-steady-state assumption in [6], disregarding the change of the longitudinal velocity of the vehicle for a short period of time. Also, the vehicle roll, pitch and yaw motion are assumed to maintain their steady states. Klomp et al. use a similar approach in [4]. Tremlett et al. in [16] and Novellis et al. in [17] additionally require that the derivative of the longitudinal slip of each wheel is zero, whereas the lateral and yaw motion fulfil the steady-state condition.

In the literature, vehicle stability properties are analysed using basic vehicle models, either assuming steady-state conditions or combined longitudinal and lateral acceleration, where stability properties are examined for specific, fixed drive or brake torque distributions.

The novelty of this paper is the incorporation of a variable drive torque distribution, an inherent feature of AWD electric vehicle powertrain architectures, to analyse its impact on the stability properties of the vehicle at combined longitudinal and lateral acceleration. Therefore, a detailed vehicle model is applied to take relevant effects like the dynamics of the individual wheels, the wheel load transfer, and the mutual influence of longitudinal and lateral tyre forces into account.

The paper is structured as follows: In the subsequent Sect. 2, the vehicle and tyre model are introduced. In Sect. 3, the used methods are briefly described. In the following Sect. 4 the handling characteristics are shown and different types of loss of stability are identified. The Takens–Bogdanov bifurcation is shown in the GG envelope and different causes of its appearance and its connection to the occurrence of a Fold bifurcation are presented. In Sect. 5, main findings are summarised and conclusions are drawn.

2 Vehicle and tyre model

To study vehicle stability properties up to high levels of both lateral and longitudinal acceleration, a nonlinear 10 degrees of freedom vehicle model is employed, Fig. 1, incorporating a nonlinear tyre model, wheel load transfer, and nonlinear steering kinematics. The road surface is represented by a horizontal plane.

The vehicle body is modelled as a rigid body with 6 degrees of freedom, with mass m and moments of inertia I_x, I_y and I_z. The products of inertia are neglected. The vehicle body is connected to the massless axles with spring stiffnesses c_k and damping d_k, $k \in \{F,\ R\}$, at the front axle and rear axle, respectively. The anti-roll bars are considered by additional stiffnesses $c_{\mathrm{r}k}$. The four individual wheels with effective moment of inertia $I_{\mathrm{W}k}$ are modelled with one rotational degree of freedom each. The vehicle parameters are listed in Table 1. These refer to an SUV vehicle and are adjusted to measurements carried out with the reference vehicle.

The tyre force characteristics are described by Pacejka's Magic Formula model [18], where tyre parameters are derived from trailer measurements and the slip stiffnesses and maximum friction values of the tyres are adjusted to fit the handling characteristics of the reference vehicle.

To reduce the complexity in the derivation of the governing equations of motion of the vehicle body, two different coordinate systems are used: the equations of motion for the rotational degrees of freedom are described in the body-fixed coordinate system (x_B-y_B-z_B), whereas the equations of the translational degrees of freedom are described in a coordinate system moved

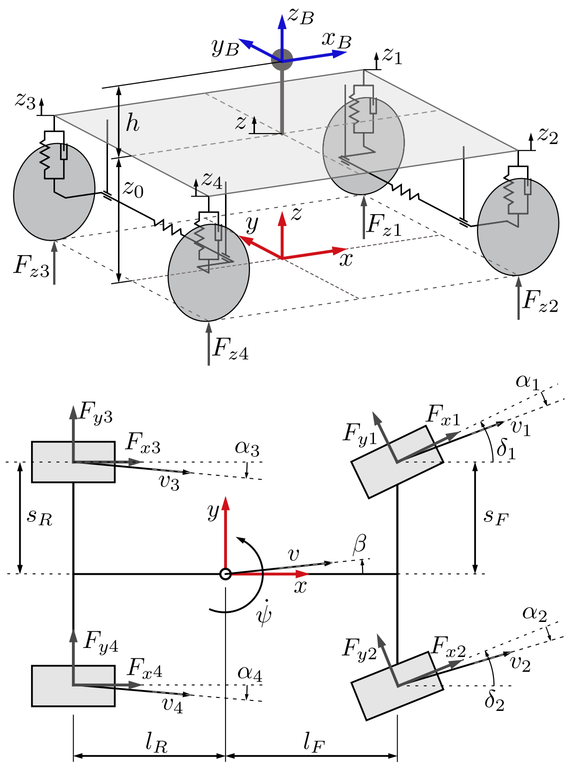

Fig. 1 Schematic illustration of the vehicle model

in the ground plane (x-y-z). The body-fixed coordinate system (x_B-y_B-z_B) is rotated relative to the ground plane with pitch angle θ and roll angle φ w.r.t. the y_B-axis and the x_B-axis, respectively. The equations of motions are derived assuming small angles φ and θ, and respective derivatives,

$$m\,(\dot{v}_x - v_y\,\dot{\psi} + h\,\ddot{\theta} + 2\,h\,\dot{\varphi}\,\dot{\psi} - h\,\theta\,\dot{\psi}^2 + h\,\varphi\,\ddot{\psi}) = \Sigma F_x \tag{1a}$$

$$m\,(\dot{v}_y + v_x\,\dot{\psi} - h\,\ddot{\varphi} + 2\,h\,\dot{\theta}\,\dot{\psi} + h\,\varphi\,\dot{\psi}^2 + h\,\theta\,\ddot{\psi}) = \Sigma F_y \tag{1b}$$

$$m\,\dot{v}_z = \Sigma F_z \tag{1c}$$

$$I_x\,\ddot{\varphi} - (I_y - I_z)\,\dot{\theta}\,\dot{\psi} = \Sigma M_x - \theta\,\Sigma M_z \tag{1d}$$

$$I_y\,\ddot{\theta} - (I_z - I_x)\,\dot{\psi}\,\dot{\varphi} = \Sigma M_y + \varphi\,\Sigma M_z \tag{1e}$$

$$I_z\,\ddot{\psi} - (I_x - I_y)\,\dot{\varphi}\,\dot{\theta} = \Sigma M_z + \theta\,\Sigma M_x - \varphi\,\Sigma M_y \tag{1f}$$

with the longitudinal velocity v_x, lateral velocity v_y, yaw rate $\dot{\psi}$, and the sum of forces ΣF_j, $j \in \{x,\ y,\ z\}$, and of moments ΣM_j:

$$\Sigma F_x = F_{x1}\cos\delta_1 - F_{y1}\sin\delta_1 + F_{x2}\cos\delta_2 - F_{y2}\sin\delta_2 + F_{x3} + F_{x4} \tag{2a}$$
$$\Sigma F_y = F_{y1}\cos\delta_1 + F_{x1}\sin\delta_1 + F_{y2}\cos\delta_2 + F_{x2}\sin\delta_2 + F_{y3} + F_{y4} \tag{2b}$$
$$\Sigma F_z = F_{z1} + F_{z2} + F_{z3} + F_{z4} - m\,\mathrm{g} \tag{2c}$$
$$\Sigma M_x = F_{z1}(s_\mathrm{F} + h\,\varphi) - F_{z2}(s_\mathrm{F} - h\,\varphi) + F_{z3}(s_\mathrm{R} + h\,\varphi) - F_{z4}(s_\mathrm{R} - h\,\varphi) + \Sigma F_y\,(h + z_0 + z) \tag{2d}$$
$$\Sigma M_y = -(F_{z1} + F_{z2})(l_\mathrm{F} - h\,\theta) + (F_{z3} + F_{z4})(l_\mathrm{R} + h\,\theta) - \Sigma F_x\,(h + z_0 + z) \tag{2e}$$
$$\begin{aligned}\Sigma M_z = \Sigma M_{z,\mathrm{tyre}} &+ (F_{y1}\cos\delta_1 + F_{x1}\sin\delta_1 + F_{y2}\cos\delta_2 + F_{x2}\sin\delta_2)(l_\mathrm{F} - h\,\theta) \\ &- (F_{y3} + F_{y4})(l_\mathrm{R} + h\,\theta) \\ &- (F_{x1}\cos\delta_1 - F_{y1}\sin\delta_1)(s_\mathrm{F} + h\,\varphi) \\ &+ (F_{x2}\cos\delta_2 - F_{y2}\sin\delta_2)(s_\mathrm{F} - h\,\varphi) \\ &- F_{x3}(s_\mathrm{R} + h\,\varphi) + F_{x4}(s_\mathrm{R} - h\,\varphi).\end{aligned} \tag{2f}$$

F_{xi}, $i \in \{1, 2, 3, 4\}$, represent the longitudinal tyre forces of the individual wheels, and F_{yi} represent the lateral tyre forces, which depend on the longitudinal tyre slips s_{xi}, sideslip angles α_i, and the vertical tyre forces F_{zi}. $\Sigma M_{z,\mathrm{tyre}}$ represents the sum of the self-aligning torques M_{zi} of the tyres. The vertical tyre forces are calculated with

$$F_{z1} = F_{z1,0} - c_\mathrm{F}\,z_1 - d_\mathrm{F}\,\dot z_1 - c_\mathrm{rF}\,(z_1 - z_2) \tag{3a}$$
$$F_{z2} = F_{z2,0} - c_\mathrm{F}\,z_2 - d_\mathrm{F}\,\dot z_2 + c_\mathrm{rF}\,(z_1 - z_2) \tag{3b}$$
$$F_{z3} = F_{z3,0} - c_\mathrm{R}\,z_3 - d_\mathrm{R}\,\dot z_3 - c_\mathrm{rR}\,(z_3 - z_4) \tag{3c}$$
$$F_{z4} = F_{z4,0} - c_\mathrm{R}\,z_4 - d_\mathrm{R}\,\dot z_4 + c_\mathrm{rR}\,(z_3 - z_4) \tag{3d}$$

where $F_{zi,0}$ represents the nominal vertical tyre forces. The wheel travels z_i are derived from the vertical displacement z of the vehicle body, the pitch angle θ and the roll angle φ,

$$z_1 = z + \varphi\,s_\mathrm{F} - \theta\,l_\mathrm{F} \tag{4a}$$
$$z_2 = z - \varphi\,s_\mathrm{F} - \theta\,l_\mathrm{F} \tag{4b}$$
$$z_3 = z + \varphi\,s_\mathrm{R} + \theta\,l_\mathrm{R} \tag{4c}$$
$$z_4 = z - \varphi\,s_\mathrm{R} + \theta\,l_\mathrm{R} \tag{4d}$$

From geometric and kinematic considerations, the tyre sideslip angles α_i are derived,

$$\tan(\delta_1 - \alpha_1) = \frac{v_y + l_\mathrm{F}\,\dot\psi}{v_x - s_\mathrm{F}\,\dot\psi} \tag{5a}$$
$$\tan(\delta_2 - \alpha_2) = \frac{v_y + l_\mathrm{F}\,\dot\psi}{v_x + s_\mathrm{F}\,\dot\psi} \tag{5b}$$
$$\tan\alpha_3 = -\frac{v_y - l_\mathrm{R}\,\dot\psi}{v_x - s_\mathrm{R}\,\dot\psi} \tag{5c}$$
$$\tan\alpha_4 = -\frac{v_y - l_\mathrm{R}\,\dot\psi}{v_x + s_\mathrm{R}\,\dot\psi} \tag{5d}$$

Ackermann steering behaviour is assumed,

$$\frac{l_\mathrm{F} + l_\mathrm{R}}{\tan\delta_1} + s_\mathrm{F} = \frac{l_\mathrm{F} + l_\mathrm{R}}{\tan\delta} \tag{6a}$$
$$\frac{l_\mathrm{F} + l_\mathrm{R}}{\tan\delta_2} - s_\mathrm{F} = \frac{l_\mathrm{F} + l_\mathrm{R}}{\tan\delta} \tag{6b}$$

with the steering angle δ and the steering angles $\delta_{1,2}$ of the front wheels.

The longitudinal tyre slips s_{xi} are defined by

$$s_{x1} = \frac{r\,\omega_1}{v_{\mathrm{W}1}} - 1 \tag{7a}$$
$$s_{x2} = \frac{r\,\omega_2}{v_{\mathrm{W}2}} - 1 \tag{7b}$$
$$s_{x3} = \frac{r\,\omega_3}{(v_x - s_\mathrm{R}\,\dot\psi)} - 1 \tag{7c}$$
$$s_{x4} = \frac{r\,\omega_4}{(v_x + s_\mathrm{R}\,\dot\psi)} - 1 \tag{7d}$$

$v_{\mathrm{W}i}$ represent the velocities of the centre of the front wheels in the direction of the respective wheel plane,

$$v_{\mathrm{W}1} = (v_x - s_\mathrm{F}\,\dot\psi)\cos\delta_1 + (v_y + l_\mathrm{F}\,\dot\psi)\sin\delta_1 \tag{8a}$$
$$v_{\mathrm{W}2} = (v_x + s_\mathrm{F}\,\dot\psi)\cos\delta_2 + (v_y + l_\mathrm{F}\,\dot\psi)\sin\delta_2 \tag{8b}$$

with the angular velocities of the wheels ω_i and tyre radius r.

The equation of motion of the wheels read

$$I_{\mathrm{W}k}\,\dot\omega_i = T_i - F_{xi}\,r, \tag{9}$$

with the effective moment of inertia $I_{\mathrm{W}k}$, $k \in \{\mathrm{F}, \mathrm{R}\}$, which represents half of the reduced moment of inertia of the respective axle. Assuming open differential gears at both the front axle and the rear axle, the drive (or brake) torque T_i of the individual wheels is given by $T_{1,2} = T_\mathrm{F}/2$ and $T_{3,4} = T_\mathrm{R}/2$, respectively.

The drive torque at the front axle and the rear axle, T_F and T_R, respectively, depends on the total drive torque T_{tot} requested by the driver (through throttle and brake pedal inputs) and the drive torque distribution γ. The drive torque distribution γ represents the ratio of the total drive torque T_{tot} that is applied to the rear axle,

$$\gamma = T_R / T_{tot}. \tag{10}$$

Consequently, the torque at the front axle and the rear axle are given by

$$T_F = (1 - \gamma)\, T_{tot} \quad \text{and} \quad T_R = \gamma\, T_{tot}. \tag{11}$$

In the figures presented in Sect. 4, instead of the longitudinal velocity v_x and the lateral velocity v_y of the origin of the x-y-z coordinate system, the velocity v and the sideslip angle β of the vehicle are depicted, were

$$v_x = v \cos\beta, \quad v_y = v \sin\beta. \tag{12}$$

This representation is more intuitive, offering a clearer understanding of the vehicle state being illustrated.

The longitudinal and lateral tyre forces, F_{xi} and F_{yi}, respectively, of the applied Magic Formula tyre model depend, as mentioned above, on the vertical tyre force F_{zi}, the tyre sideslip angle α_i, and the longitudinal slip s_{xi}. The influence of the camber angle is neglected.

In Fig. 2 the normalized lateral tyre forces $F_{yi}/F_{zi,0}$ are shown over the normalized longitudinal tyre forces $F_{xi}/F_{zi,0}$ for constant sideslip angles α. The characteristics of a front tyre are shown in solid lines and the characteristics of a rear tyre are shown in dash-dotted lines.

Examining the pure lateral tyre characteristics (i.e. the points where $F_{xi}/F_{zi,0} = 0$ for different values of α in Fig. 2) shows that the cornering stiffness of the front tyres is lower than the cornering stiffness of the rear tyres, due to different tyre dimensions considered. Both the maximum lateral and the longitudinal friction potentials are higher at the rear tyres compared to the front tyres.

With increasing longitudinal slip, the (local) cornering stiffness of the tyres decreases, significantly affecting the vehicle's handling and stability properties under combined lateral and longitudinal tyre slip conditions.

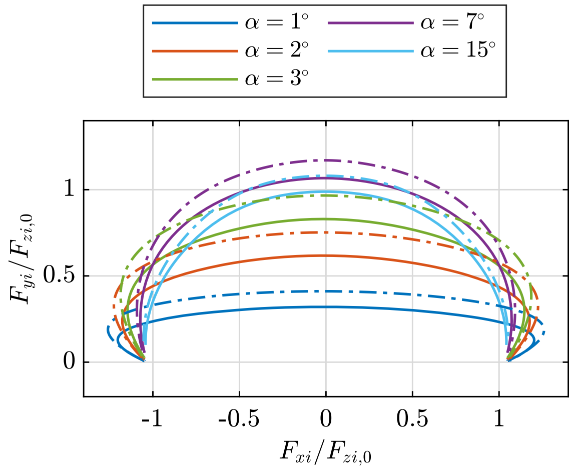

Fig. 2 Combined normalized tyre forces for constant sideslip angles α and varied longitudinal slip s_x for a front tyre, $i \in \{1, 2\}$ (solid lines), and a rear tyre, $i \in \{3, 4\}$ (dashed lines)

3 Methods

To analyse the impact of the drive torque distribution γ on the stability properties of the vehicle during manoeuvres with combined lateral and longitudinal acceleration, the transient state ($a_n \neq 0, a_t \neq 0$) is transformed to a quasi-steady-state that approximates the transient condition well, [4,5,16,17].

3.1 Quasi-steady-state description

Here, a similar approach to Horiuchi et al. [5] is used, where an equivalent longitudinal force is applied in the vehicle's longitudinal axis at the centre of gravity to transform the transient state during acceleration and braking into an equivalent equilibrium state. The derivative of the velocity of the vehicle, $\dot{v}$, is set to the desired tangential acceleration a_t. This adjustment is equivalent to applying an inertial force acting at the centre of gravity of the vehicle in the opposite direction of the velocity v. As a result, both the wheel load transfer and the longitudinal tyre forces required to achieve the desired tangential acceleration a_t are taken into account, allowing the vehicle to be considered in a steady-state condition.

The yaw acceleration $\ddot{\psi}$, the derivative of the vehicle sideslip angle $\dot{\beta}$, and the derivatives of the other states are set to zero to satisfy the steady-state condition. In contrast to [16] and [17], not the derivative of longitu-

Table 1 Parameters of the vehicle model

Parameter	Value	Unit	Description
m	2550	kg	Total mass of the vehicle
I_x	950	$\mathrm{kg\,m^2}$	Moment of inertia about the x-axis
I_y	3400	$\mathrm{kg\,m^2}$	Moment of inertia about the y-axis
I_z	3600	$\mathrm{kg\,m^2}$	Moment of inertia about the z-axis
I_{WF}	3.3	$\mathrm{kg\,m^2}$	Effective moment of inertia of one front wheel
I_{WR}	8	$\mathrm{kg\,m^2}$	Effective moment of inertia of one rear wheel
l_{F}	1.5	m	Length from the centre of gravity to the front axle
l_{R}	1.4	m	Length from the centre of gravity to the rear axle
s_{F}	0.84	m	Half of the track width at the front axle
s_{R}	0.83	m	Half of the track width at the rear axle
z_0	0.13	m	Height z_0
h	0.42	m	Height h
r	0.367	m	Radius of the tyre
c_{F}	2.5×10^4	N/m	Spring stiffness at the front axle
c_{R}	2.6×10^4	N/m	Spring stiffness at the rear axle
d_{F}	5×10^3	N/(m s)	Damping constant at the front axle
d_{R}	5×10^3	N/(m s)	Damping constant at the rear axle
c_{rF}	3.5×10^4	N/m	Roll stiffness at the front axle
c_{rR}	3.2×10^4	N/m	Roll stiffness at the rear axle

dinal tyre slips $\dot{s}_{xi}$ but the angular acceleration of the wheels $\dot{\omega}_i$ are set to zero.

3.2 Stability of first order

Once a solution of the nonlinear quasi-steady-state system is found, the nonlinear equations of motion are linearised w.r.t. this steady state, $\Delta\dot{\mathbf{x}} = \mathbf{A}\,\Delta\mathbf{x} + \mathbf{B}\,\Delta\mathbf{u}$, with state vector $\Delta\mathbf{x}$ and (fixed) control parameter vector $\Delta\mathbf{u}$, and system matrix $\mathbf{A}$ and input matrix $\mathbf{B}$. Lyapunov's first method implies that a steady state is stable if all eigenvalues of $\mathbf{A}$ have negative real parts, [19]. If one or more eigenvalues have a positive real part, the steady state is unstable. If one or more eigenvalues have a zero real part while all the other eigenvalues have a negative real part, the steady state is at the stability limit. The configuration and number of the eigenvalues with zero real part determine the type of bifurcation emerging from this steady state.

3.3 Bifurcation analysis and continuation algorithm

Bifurcation analysis refers to the study of changes in the structure or stability of the solutions of a system as parameters are varied, [19–22]. With the help of a path continuation algorithm, solution paths are found by varying a distinguished parameter. To conduct a bifurcation analysis, the system to be investigated is described by the dynamics equation

$$\dot{\mathbf{x}}(t) = \mathbf{f}(\mathbf{x},\ \mathbf{p}) \tag{13}$$

where $\mathbf{x}$ represents the state vector of the vehicle model and $\mathbf{p}$ is the vector of parameters. In this study the parameter vector consists of $\mathbf{p} = [\delta,\ T_{\mathrm{tot}},\ \gamma,\ a_t]^{\mathrm{T}}$. The parameter vector is split into a distinguished parameter λ, e.g. the drive torque distribution γ, and free and fixed parameters $\mathbf{p}_{\mathrm{free}}$ and $\mathbf{p}_{\mathrm{fixed}}$, respectively.

It is intended to investigate different (quasi-steady-state) driving conditions for the same vehicle velocity for a varied distinguished parameter. Hence, the vehicle velocity is fixed, here to a selected value of $v = v_0 = 20\,\mathrm{m/s}$. Therefore constraint equations are required, and the augmented set of equations reads as follows:

$$\dot{\mathbf{x}}(t) = \mathbf{f}(\mathbf{x},\ \mathbf{p}), \quad \mathbf{g}(\mathbf{x},\ \mathbf{p}) = \mathbf{0}. \tag{14}$$

where

$$\mathbf{g}(\mathbf{x},\ \mathbf{p}) = \begin{bmatrix} v - v_0 \\ \mathbf{p}_l - \mathbf{p}_{\text{fixed}} \end{bmatrix} \tag{15}$$

with the indices l of the fixed parameters. If, in addition to the velocity v, further states shall be fixed, a respective number of fixed parameters from $\mathbf{p}_{\text{fixed}}$ must instead be incorporated into $\mathbf{p}_{\text{free}}$.

For path continuation, the algorithm tracks the solution path by 'tangential continuation', utilizing the current and prior found solution to make an initial guess for the next solution step, [20]. To track solution paths of bifurcation points, additional constraint equations related to the respective type of bifurcation (e.g. Hopf, Fold and Takens–Bogdanov bifurcation), [19–22], have to be considered, where, depending on the codimension of the corresponding bifurcation, [19], the respective number of fixed parameters have to be set free.

4 Results

4.1 Steady-state handling characteristics

Vehicle and tyre parameters have been selected to map a vehicle with understeering characteristics, [18], at zero tangential acceleration $\dot{v} = a_t = 0\,\text{m/s}^2$, see also Sect. 2. The handling diagram for $\gamma = 0$ (FWD configuration) and $\gamma = 1$ (RWD configuration) is depicted in the top graph of Fig. 3, where the steering angle δ is plotted over the steady-state normal acceleration $a_n = v\,\dot{\psi}$ at a constant vehicle velocity of $v = 20\,\text{m/s}$. Moreover, at high normal acceleration, both configurations show final understeer characteristics, [23]. Consequently, various AWD configurations (i.e. $0 < \gamma < 1$) will show similar (final) understeer characteristics. Due to zero tangential acceleration a_t and small vehicle sideslip angles β, the longitudinal load transfer is almost zero.

Since the traction forces at the front wheels generate additional yaw torque in the FWD configuration due to the steered front wheels, a slightly higher maximum normal acceleration may be observed compared to RWD configuration, see also [8]. This effect decreases with increasing vehicle velocities since the steering angle at the maximal normal acceleration decreases.

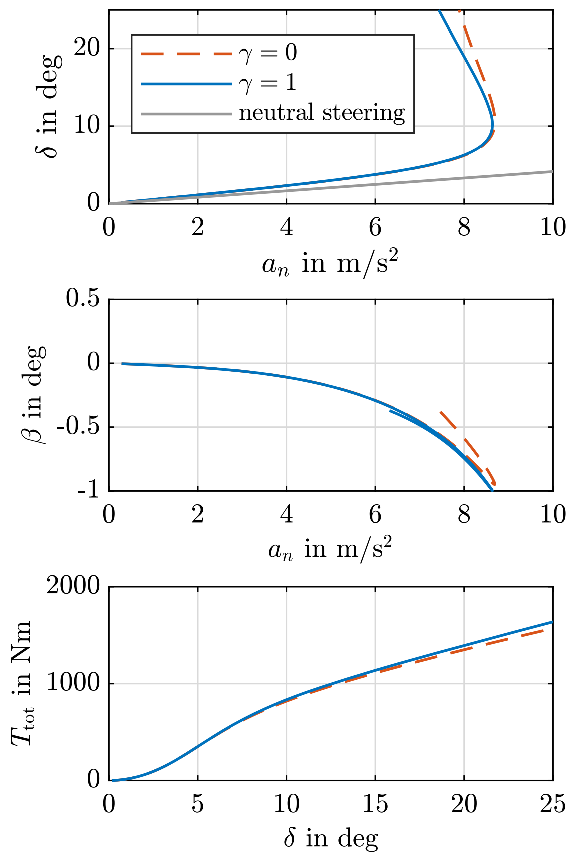

Fig. 3 Handling diagram of the front and rear-drive vehicle at zero tangential acceleration $a_t = 0\,\text{m/s}^2$ and constant velocity $v = 20\,\text{m/s}$, compared to neutral steering behaviour

In the middle graph of Fig. 3, the evolution of the vehicle sideslip angle β is depicted. It may be noticed that at the FWD configuration, the absolute value of the vehicle sideslip angle β decreases after reaching the maximum normal acceleration. In contrast, at the RWD configuration, the sideslip angles β remain similar. This effect can also be attributed to the longitudinal forces at the front axle. The steady-state total drive torque T_{tot} is plotted over the steering angle δ at the bottom graph in Fig. 3. After reaching the maximum normal acceleration a_n at $\delta \approx 10$ deg, slightly higher total drive torques T_{tot} result at the RWD configuration compared to the FWD configuration.

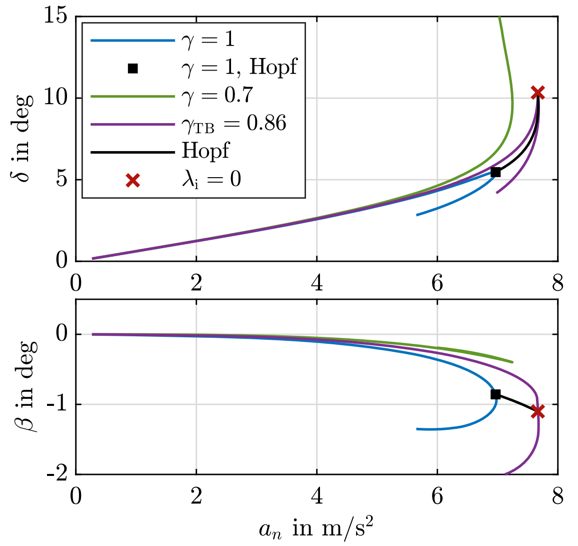

Fig. 4 Steering angle δ and vehicle sideslip angle β for different drive torque distributions γ plotted over the normal acceleration a_n. Quasi-steady-state solutions for tangential acceleration $a_t = 4\,\text{m/s}^2$ and constant velocity $v = 20\,\text{m/s}$

4.2 Handling behaviour under longitudinal acceleration

Increasing the vehicle tangential acceleration a_t results in a qualitative change in the handling characteristics of the vehicle with the RWD configuration, $\gamma = 1$, compared to the zero tangential acceleration case. The handling diagram in Fig. 4 is derived for a constant tangential acceleration $a_t = 4\,\text{m/s}^2$, which corresponds to a medium tangential acceleration on a high friction road surface. The handling characteristics change to final oversteer behaviour at a certain normal acceleration, Fig. 4, blue line. In contrast, for an AWD configuration with a considerable portion of the total drive torque T_{tot} at the front axle, e.g. $\gamma = 0.7$, the final understeer characteristics are maintained, green line.

At evaluating the eigenvalues of the $\gamma = 1$ branch at $a_t = 4\,\text{m/s}^2$, a Hopf-type loss of stability is identified close to the maximum normal acceleration $a_n \approx 7\,\text{m/s}^2$, marked with a black square in Fig. 4. Similar findings are presented in [24–26] for vehicles with oversteering characteristics in steady-state conditions. The Hopf bifurcation indicates an oscillatory loss of stability, in this case with very low frequency up to approximately 0.05 Hz. The critical mode shape of the Hopf bifurcation is described in [24] for a three degrees of freedom two-wheel vehicle model. It was shown that the velocity v and yaw rate $\dot{\psi}$ represent the dominant entries of the eigenvector. With the extended vehicle model applied in this study, additionally, the angular speed of the rear inner wheel ω_3 significantly contributes to the eigenvector of the critical mode.

To derive the Hopf branch in the handling diagram depicted in Fig. 4, the drive torque distribution γ is selected to be the distinguished parameter. The solution of the Hopf branch is calculated for constant tangential acceleration $a_t = 4\,\text{m/s}^2$. With decreasing drive torque distribution γ, the Hopf point, starting at the black square in Fig. 4 with $\gamma = 1$, moves to higher normal accelerations a_n, black line, until the imaginary part of the Hopf eigenvalue λ_{i} approaches zero, indicated by the red $\times$. The period of the limit cycle related to the Hopf bifurcation increases towards infinity, and the loss of stability transitions from oscillatory to non-oscillatory. For the considered vehicle model and parameters, and for a tangential acceleration of $a_t = 4\,\text{m/s}^2$, this condition is reached at $\gamma = \gamma_{\text{TB}} = 0.86$.

For $\lambda_{\text{i}} = 0$ a new type of bifurcation occurs, characterised by a double zero eigenvalue, known as the Takens–Bogdanov bifurcation. This type of bifurcation was reported in [11] for a pure lateral two degrees of freedom two-wheel vehicle model, and it is characterised by reaching the maximum lateral axle force of the front axle and the rear axle simultaneously. As a result, a small change in the vehicle state will not result in a change in the lateral axle forces both at the front axle and the rear axle. In the detailed vehicle model used in this study, the Takens-Bogdanov point has the property that either the lateral force or the longitudinal force of the front axle and the rear axle reach their maximum simultaneously. This will be discussed in more detail in Sect. 4.4.

A further decrease of the drive torque distribution γ ($< \gamma_{\text{TB}}$) results in a final understeer handling characteristics of the vehicle. Therefore the Takens–Bogdanov point defines the change from final oversteer to final understeer behaviour.

For a given tangential acceleration, e.g. $a_t = 4\,\text{m/s}^2$ in Fig. 4, there exists only one quasi-steady-state solution with a double zero eigenvalue, i.e. the Takens–Bogdanov point.

4.3 GG envelope

From the handling diagram Fig. 4, it becomes obvious that the Takens–Bogdanov point, red ×, represents a quasi-steady-state driving condition very close to the maximum attainable normal acceleration a_n of the vehicle for a given tangential acceleration a_t. Moreover, it defines the maximum normal acceleration a_n of stable steady-state driving conditions in the vehicle handling characteristics for the drive torque distribution γ_{TB}, due to the double zero eigenvalue, purple line in Fig. 4.

Hence, by varying the tangential acceleration a_t, the corresponding normal acceleration a_n at the Takens–Bogdanov points defines a GG envelope of the vehicle close to the maximum attainable GG envelope found with optimisation technique [27]. However, the GG envelope defined by the Takens–Bogdanov branch represents the maximum GG envelope of stable steady-state driving conditions.

In Fig. 5, the GG envelope is plotted w.r.t. the longitudinal and lateral acceleration of the vehicle, a_x and a_y, respectively, as is typical for a GG diagram, [28]. Since this diagram is symmetrical w.r.t. the abscissa, it is plotted and discussed for $a_y \geq 0\,\mathrm{m/s^2}$ only in the following. At longitudinal accelerations $a_x \approx 3\,\mathrm{m/s^2}$ to $12\,\mathrm{m/s^2}$ and decelerations $a_x \approx -2\,\mathrm{m/s^2}$ to $-12\,\mathrm{m/s^2}$, Takens–Bogdanov branches exist and are plotted in red colour. Between $a_x \approx -2\,\mathrm{m/s^2}$ and $a_x \approx 3\,\mathrm{m/s^2}$, the vehicle exhibits final understeer behaviour for several drive torque distributions γ, where the maximum attainable normal accelerations a_y for $\gamma = 1$ is depicted in Fig. 5, blue colour. Obviously, the maximum attainable lateral accelerations a_y increase with decreasing a_x between the onsets of the Takens–Bogdanov branches. This property of the GG envelope may be attributed to the longitudinal load transfer between the axles, which increases the vertical load at the front ('weaker') axle for decreasing a_x, and consequently enhances transferable tyre forces.

At $a_x \approx 3\,\mathrm{m/s^2}$, besides the Takens–Bogdanov branch, also a Hopf bifurcation emerges, both for a drive torque distribution of $\gamma = 1$, see p_1 indicated by the blue × in Fig. 5, and similar at $a_x \approx -2\,\mathrm{m/s^2}$. Beyond longitudinal accelerations $a_x \approx 3\,\mathrm{m/s^2}$, the Hopf branch for $\gamma = 1$ (grey solid line in Fig. 5) limits the 'stable' area of combined accelerations for the RWD configuration, similarly for negative a_x. The Hopf bifurcation exists for final oversteer vehicle configurations, which is equivalent to a drive torque distribution between $\gamma = 1$ and the drive torque distribution γ_{TB} of the Takens–Bogdanov point, for a given longitudinal acceleration a_x.

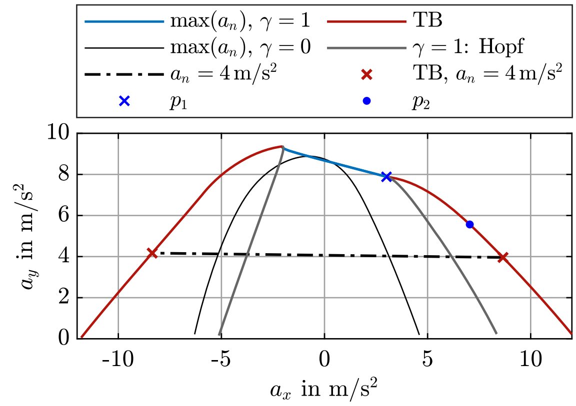

Fig. 5 Takens–Bogdanov and Hopf branches in the GG diagram

The black line in Fig. 5 shows the maximum attainable combined lateral and longitudinal accelerations for drive and brake forces applied at the front axle only ($\gamma = 0$). It can be observed that in the acceleration case, $a_x > 0$, the configuration with $\gamma = 1$ is superior compared to $\gamma = 0$ considering the GG envelope, with the opposite in the deceleration case. However, the (stable) GG envelope for both $\gamma = 1$ and $\gamma = 0$ is considerably smaller compared to the Takens–Bogdanov configuration $\gamma = \gamma_{\mathrm{TB}}$.

The drive torque distribution γ_{TB} along both Takens–Bogdanov branches is plotted in Fig. 6 over the longitudinal acceleration a_x. For longitudinal accelerations $a_x > 0$, starting at $a_x \approx 3\,\mathrm{m/s^2}$ and $\gamma_{\mathrm{TB}} = 1$, the drive torque distribution γ_{TB} decreases initially rather strongly. For higher levels of longitudinal acceleration ($a_x \gtrsim 6\,\mathrm{m/s^2}$), the drive torque distribution γ_{TB} remains almost constant. This qualitative change arises from the fact that the appearance of the Takens-Bogdanov bifurcation may have various causes that will be investigated in Sect. 4.4 by inspecting the corresponding tyre forces. In the deceleration case ($a_x < 0$), the evolution of the drive torque distribution γ_{TB} over a_x exhibits qualitatively similar behaviour. However, at high levels of deceleration, the value of γ_{TB} is considerably lower, at ≈ 0.3. This value is typical for the brake force distribution that ensures optimal braking performance, see [29].

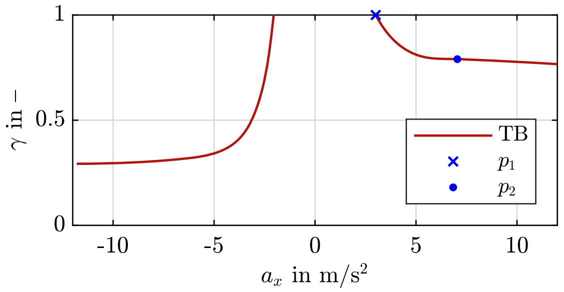

Fig. 6 Drive torque distribution γ_{TB} of the Takens–Bogdanov branch plotted over longitudinal acceleration a_x

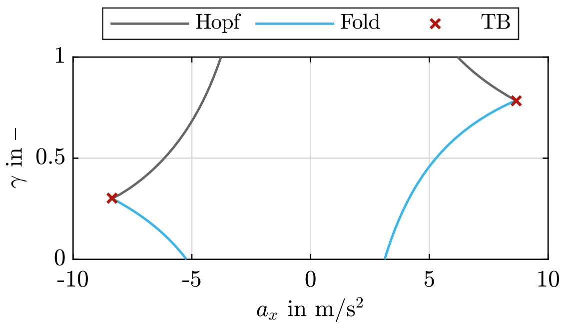

Fig. 7 Hopf and Fold bifurcation in the γ-a_x-plane for a normal acceleration of $a_n = 4\,\mathrm{m/s}^2$ corresponding to the dash-dotted line in Fig. 5

For drive torque distributions $\gamma < \gamma_{\mathrm{TB}}$, e.g. FWD vehicles, and a certain level of longitudinal acceleration $|a_x|$, another type of loss of stability is found: a Fold bifurcation. The Fold bifurcation is, similar to the Hopf bifurcation, a codimension one bifurcation. It is characterised by a single zero eigenvalue.

To illustrate how the stability boundaries, defined by the Hopf, Takens–Bogdanov, and Fold bifurcations, evolve depending on the drive torque distribution γ for a specific level of normal acceleration a_n ($\approx a_y$), a corresponding contour plot is indicated as a black dash-dotted line in the GG diagram Fig. 5 and plotted in Fig. 7.

For the $\gamma = 0$ configuration and $a_n = 4\,\mathrm{m/s}^2 =$ const, at $a_x \approx 3\,\mathrm{m/s}^2$ and $a_x \approx -5\,\mathrm{m/s}^2$, Fold bifurcations occur, characterised by a non-oscillatory loss of stability. The corresponding critical eigenvector indicates a spin-up of the front inner wheel, where the global motion of the vehicle in the road plane is only marginally affected. By increasing the drive torque distribution γ, the Fold bifurcation branches reach the Takens–Bogdanov points, red $\times$ in Fig. 7. A second eigenvalue (besides the zero eigenvalue of the Fold bifurcation) converges to zero approaching the Takens–Bogdanov points. Increasing the drive torque distribution γ further ($\gamma > \gamma_{\mathrm{TB}}$), the Hopf bifurcation branches define the stability boundary, where the double zero eigenvalues change to conjugate complex eigenvalue pairs, and the configuration results in a final oversteer vehicle behaviour.

Obviously, for a desired constant lateral acceleration a_y, the drive torque distribution γ_{TB} allows for maximum longitudinal acceleration a_x within the stable GG envelope.

The most relevant parameter defining the GG envelope is the friction potential since the stability boundaries strongly depend on the saturation of the tyre forces. A different friction potential basically scales the GG diagram. At low friction surfaces, due to lower levels of acceleration and consequently vertical load transfer, lower drive torque distributions result for the Takens-Bogdanov branch for positive longitudinal acceleration. The branch is shifted, but the qualitative behaviour does not change.

Besides the Takens–Bogdanov bifurcation, characteristic properties of the Fold bifurcation are investigated in more detail in the next sections, focusing on practical implications.

4.4 Interpretation from a vehicle dynamics perspective

To allow for an interpretation of the Takens–Bogdanov branch from a vehicle dynamics perspective, the operating conditions of the tyres are inspected at two representative vehicle states in the following.

In Figs. 8 and 9, the longitudinal and lateral tyre forces are shown for two characteristic Takens–Bogdanov points, p_1 and p_2 (see Figs. 5 and 6). In the left graphs, the normalized longitudinal tyre forces $F_{xi}/F_{zi,0}$, $i \in \{1, 2, 3, 4\}$ are plotted against the longitudinal slips s_{xi} for the constant sideslip angles α_i corresponding to p_1 and p_2, respectively. In the right graphs, the normalized lateral tyre forces $F_{yi}/F_{zi,0}$ plotted against the sideslip angles α_i are depicted for respective longitudinal slips s_{xi}. The tyre forces at the investigated Takens–Bogdanov points are indicated by $\circ$.

Since $\gamma = \gamma_{\mathrm{TB}} = 1$ at p_1, the normalized longitudinal tyre forces $F_{xi}/F_{zi,0}$ at the front axle are zero in

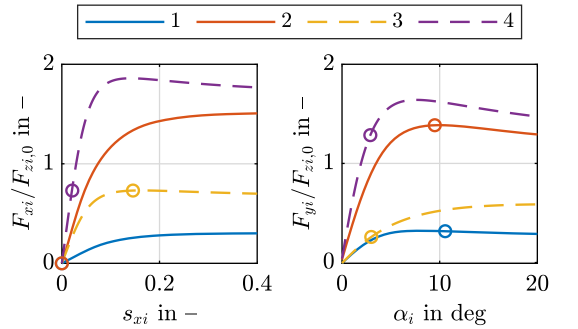

Fig. 8 Tyre characteristics corresponding to p_1 ($\gamma = 1$, $a_t \approx 2.8\,\mathrm{m/s^2}$)

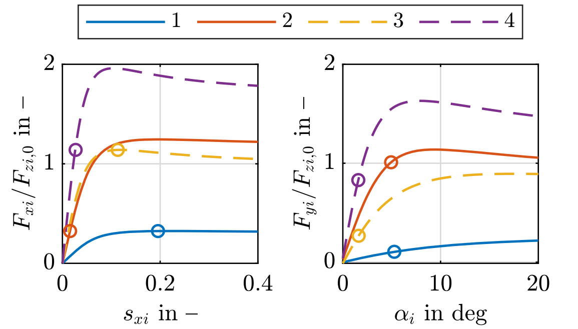

Fig. 9 Tyre characteristics corresponding to p_2 ($\gamma = 0.79, a_t = 7\,\mathrm{m/s^2}$)

Fig. 8 (left graph). The double zero eigenvalue at this Takens–Bogdanov point can be attributed to the vanishing effective (local) cornering stiffness of the front axle, caused by the saturation of the effective lateral axle force, $i \in \{1, 2\}$ (right graph) and the saturation of the longitudinal force of the inner wheel at the rear axle $i = 3$ (left graph), similar to findings presented in [11]. Consequently, due to the differential gear at the rear axle, a small variation of the slips of the tyres $i \in \{1, 2, 3\}$ does not result in a change of the respective axle forces. The post-critical behaviour of the vehicle after loss of stability is characterised by a wheel spin-up of the inner wheel at the rear axle ($i = 3$).

A different observation can be made by inspecting the tyre forces at the Takens–Bogdanov point p_2, where rather small gradients of γ w.r.t. the longitudinal acceleration a_x may be noted in Fig. 6. Compared to p_1, due to the increased portion of the total drive torque T_{tot} at the front axle (i.e. $\gamma < 1$), the inspection of the tyre forces shows that both the inner wheel at the front axle $i = 1$ and the inner wheel at the rear axle $i = 3$ reach their longitudinal force saturation simultaneously, Fig. 9 (left graph). Similar to the above, a small variation of the longitudinal slips of the tyres $i \in \{1, 3\}$ does not result in a change of the respective axle forces, due to the differential gears, resulting in a double zero eigenvalue. In the case of loss of stability, the inner wheels at both the front and rear axle may spin up.

An increase of the drive torque distribution $\gamma > \gamma(p_2)$ leads to a final oversteer behaviour of the vehicle and a Hopf bifurcation, see Fig. 7, since the tyre forces at the rear axle, $i \in \{3, 4\}$, are saturated first. Contrary, a reduction of the drive torque distribution $\gamma < \gamma(p_2)$ will result in a saturation of the longitudinal tyre force of the front inner wheel, $i = 1$, which is characterised by a single zero eigenvalue, the Fold bifurcation. This behaviour seems reasonable when inspecting the tyre forces at the Takens–Bogdanov point p_2. A corresponding handling diagram for the latter case is exemplarily shown in Fig. 10 for $a_t = 7\,\mathrm{m/s^2}$ and $\gamma = 0.75 < \gamma(p_2)$ (blue line), where a Fold bifurcation occurs directly after reaching the maximum normal acceleration. The location of the corresponding Fold point is denoted $p_2^\star$ and marked by a black dot. Loss of stability is characterised by the spin-up of the front inner wheel, $i = 1$.

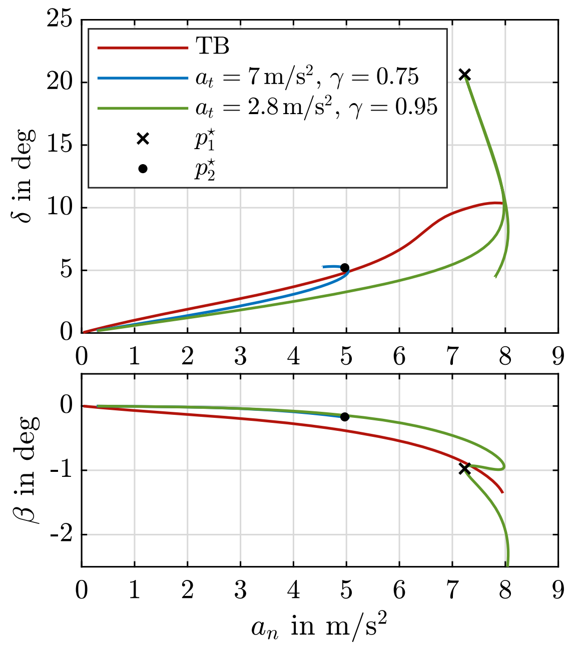

Fig. 10 Handling characteristics for different constant tangential accelerations a_t and drive torque distributions γ, with Takens–Bogdanov branch and Fold points

In contrast, at the Takens–Bogdanov point p_1, longitudinal forces at the front axle, $i \in \{1, 2\}$, are zero, see Fig. 8, since $\gamma = 1$. Consequently, the loss of stability at the corresponding Fold bifurcation for $\gamma < \gamma(p_1)$ and $a_t = a_t(p_1) = 2.8\,\mathrm{m/s^2}$ will not be characterised by a spin-up of the front inner wheel $i = 1$. The handling diagram for $a_t = a_t(p_1)$ and $\gamma = 0.95 < \gamma(p_1)$ shows 'final understeer' characteristics, Fig. 10 (green line). At the maximum steering angle $\delta \approx 21$ deg, a Fold bifurcation occurs, where the loss of stability is characterised by the spin-up of the inner wheel at the rear axle $i = 3$, similar to p_1. The corresponding Fold point is denoted $p_1^\star$ and marked by a black $\times$. The following (unstable) quasi-steady vehicle states show final oversteer characteristics. This behaviour is caused from the increased curvature resistance due to the increasing steering angle δ and consequent increase of the necessary total drive torque T_{tot}, causing the saturation of the longitudinal force at the rear axle. A further reduction of the drive torque distribution, e.g. to $\gamma = 0.9$, shifts the corresponding Fold bifurcation to even higher steering angles $\delta > 35$ deg, where the qualitative handling characteristics remain similar to the $\gamma = 0.95$ configuration (green line in Fig. 10). However, due to the large steering angles δ, this case is of less relevance from a practical perspective.

The steering angles δ and vehicle sideslip angles β corresponding to the Takens–Bogdanov branch are depicted in Fig. 10 in red colour.

Consequently, compared to the post-critical behaviour of the vehicle after the loss of stability caused by the Hopf bifurcation, see [25], the loss of stability caused by the Takens–Bogdanov and Fold bifurcation, were $\gamma \le \gamma_{\mathrm{TB}}$, is less severe from a vehicle dynamics perspective.

4.5 Fold bifurcation in the GG–γ diagram

To interpret the above Fold points $p_1^\star$ and $p_2^\star$ in the context of the GG diagram Fig. 5, the occurrence of Fold bifurcations is illustrated in a three-dimensional figure for positive longitudinal accelerations a_x, the GG–γ diagram, Fig. 11. In addition, the contour plot at $a_n = 4\,\mathrm{m/s^2}$, Fig. 7, is represented by the light grey shaded plane. For completeness, the Takens–Bogdanov branch and points p_1 and p_2 (blue $\times$ and dot), the Hopf branch for $\gamma = 1$ (grey line), and the maximum attainable normal acceleration for $\gamma = 1$ and $\gamma = 0$ (blue and black line), corresponding to Fig. 5, are depicted.

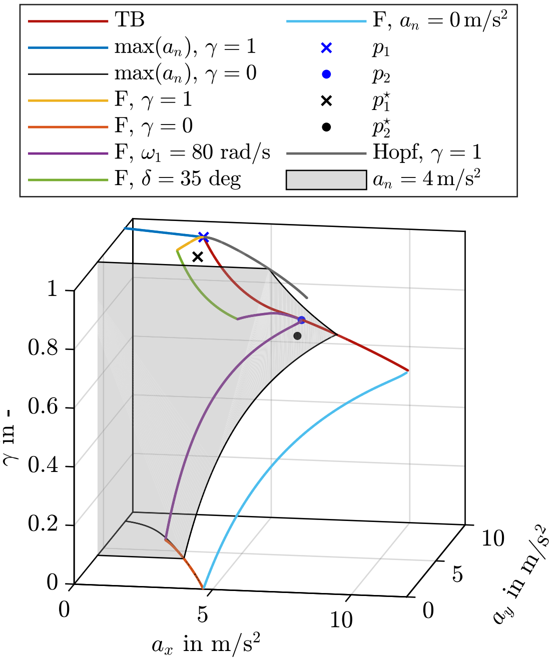

Fig. 11 Fold bifurcations in the GG–γ diagram ($a_x > 0\,\mathrm{m/s^2}$)

As described above, for a constant tangential acceleration a_t, at reducing the drive torque distribution $\gamma < \gamma_{\mathrm{TB}}$ and starting from the corresponding Takens–Bogdanov point, a Fold point is found, i.e. $p_1 \to p_1^\star$ and $p_2 \to p_2^\star$. Since in Sect. 4.4 two qualitatively different types of Fold points are identified from a vehicle dynamics perspective, $p_1^\star$ and $p_2^\star$, an illustration of the areas, where these two different types of Fold points appear in the GG–γ-diagram, is attempted.

To represent the Fold surface related to the Fold point $p_2^\star$ (black dot), where the loss of stability is characterised by the spin-up of the front inner wheel $i = 1$, four bounds are considered. One bound is defined by the Takens–Bogdanov branch (red line). The second bound is defined by the Fold branch for $a_n = 0\,\mathrm{m/s^2}$ (light blue line) that consequently is located at the $\gamma - a_x$-plane of Fig. 11. The third bound is represented by the Fold branch found for $\gamma = 0$ (orange line), i.e. a FWD vehicle, that is located at the $a_x - a_y$-plane. As this branch is continued toward higher lateral accelerations, Fold points are found that are characterised by extremely high longitudinal slips ($s_{x1} \gg 1$) at the front inner tyre, $i = 1$, while the lateral acceleration a_y

ceases to increase further. To determine the Fold surface for practical useful states, the fourth Fold branch is calculated for a constant wheel speed of the front inner wheel of $\omega_1 = 80\,\mathrm{rad/s}$ (purple line), where the longitudinal slip s_{x1} is limited to ≈ 0.25. Several Fold points located at this surface show similar behaviour w.r.t. the loss of stability.

The second Fold surface depicted in Fig. 5 is related to the Fold point $p_1^\star$ (black $\times$), where the loss of stability is characterised by the spin-up of the rear inner wheel $i = 3$ (at rather large steering angles δ). Besides the Takens–Bogdanov branch (red line), this surface again is bounded by the Fold branch calculated for a constant wheel speed of the front inner wheel of $\omega_1 = 80\,\mathrm{rad/s}$ (purple line). Starting again at the Takens–Bogdanov branch, following the third Fold branch for $\gamma = 1$ (orange line), i.e. a RWD vehicle, leads to an increase of the steering angle δ beyond practical meaningful steering angles $\delta > 35\,\mathrm{deg}$, with a handling characteristics similar as depicted in Fig. 10 for the Fold point $p_1^\star$. Consequently, the fourth Fold branch is found considering a constant steering angle $\delta = 35\,\mathrm{deg}$ (green line), taking kinematic limitations of the steering system into account.

Finally, the practical relevance of the two characteristic Fold surfaces related to $p_1^\star$ and $p_2^\star$ is investigated from a vehicle dynamics perspective. Considering the Fold surface related to $p_2^\star$, the maximum attainable normal acceleration a_n for $\gamma = 0$ in Fig. 11 (black line in the $a_x - a_y$-plane) is compared to the Fold branch for $\gamma = 0$, i.e. an FWD vehicle (orange line). The Fold branch is located close to the line characterising the maximum attainable normal acceleration. This is also obvious from inspecting the Fold point $p_2^\star$ (black dot) for $\gamma = 0.75$ in the handling diagram Fig. 10, where the maximum attainable normal acceleration a_n at a given tangential acceleration a_t is located next to $p_2^\star$. Consequently, conditions, where the loss of stability is characterised by the wheel spin-up of the front inner wheel $i = 1$, are very likely to appear in practical driving scenarios, considering parameter and state disturbances. In contrast, regarding the Fold surface related to $p_1^\star$, several respective handling diagrams are qualitatively similar to the diagram depicted in Fig. 10, $a_t = a_t(p_1) = 2.8\,\mathrm{m/s^2},\ \gamma = 0.95$ (green line). Obviously, the Fold point (black $\times$) emerges at a considerably larger steering angle δ and lower level of normal acceleration a_n compared to the maximum attainable normal acceleration in the vicinity of the Takens–Bogdanov branch (red line). Consequently, the second Fold surface is considered to be of less practical relevance.

5 Conclusions

In this paper, the impact of the drive torque distribution between the front axle and rear axle of an AWD vehicle on its combined lateral and longitudinal handling envelope and on respective stability properties has been investigated. For that purpose, bifurcation and continuation methods have been applied to a four-wheel vehicle model. Some of the main conclusions of the present research are:

- Regarding the critical mode shapes, a rather detailed vehicle and tyre model has to be considered in a simulation study on the stability properties of a vehicle at the limits of handling in regular driving to map both the 'global' vehicle motion and the dynamics of the individual wheels.
- Takens–Bogdanov bifurcations appear at the limits of handling and characterise the change from final oversteer to final understeer.
- Besides the Takens–Bogdanov bifurcations, corresponding Hopf bifurcations, [25], and Fold bifurcations are found. The drive torque distributions at the Takens–Bogdanov branch determine the transition from Hopf to Fold bifurcations.
- The Takens–Bogdanov branch also defines the drive torque distribution for reaching the maximum possible combined longitudinal and lateral acceleration envelope within the (open loop) stable steady-state handling regime, which is quite similar to the optimal, partially unstable envelope shown in [27].
- Two distinct Fold surfaces are identified that are related to the tyre operating conditions at the corresponding Takens-Bogdanov bifurcations. These Fold surfaces exhibit different, characteristic types of loss of stability, where one of these surfaces is considered to be of practical relevance.
- The drive torque distributions at the Takens–Bogdanov branch provide a good indication for a design criterium for safe and performant drive torque distribution controllers of AWD vehicles.

The approach presented in this paper to investigate the stability and handling properties of AWD vehicles at combined longitudinal and lateral accelerations will be applied to different drive architectures (e.g. including a torque vectoring system, limited-slip and locked differential gears) in future research. Moreover, an appropriate drive torque control strategy shall be developed and tested on an experimental vehicle.

Acknowledgements The authors thank Alois Steindl for the support and discussion to find and trace the bifurcation branches. The authors acknowledge TU Wien Bibliothek for financial support through its Open Access Funding Program.

Author contributions All authors contributed to the study conception and design. The analysis was performed by M.E. All authors read and approved the final manuscript.

Funding Open access funding provided by TU Wien (TUW). Open access funding provided by TU Wien (TUW).

Data availability No datasets were generated or analysed during the current study.

Declarations

Competing interests The authors declare no competing interests.

References

1. Pacejka, H.B.: Simplified analysis of steady-state turning behaviour of motor vehicles. Part 1. Handling diagrams of simple systems. Veh. Syst. Dyn. **2**(3), 161–172 (1973). https://doi.org/10.1080/00423117308968439
2. Pacejka, H.B.: Simplified analysis of steady-state turning behaviour of motor vehicles part 2: stability of the steady-state turn. Veh. Syst. Dyn. **2**(4), 173–183 (1973). https://doi.org/10.1080/00423117308968440
3. Pacejka, H.B.: Simplified analysis of steady-state turning behaviour of motor vehicles part 3: more elaborate systems. Veh. Syst. Dyn. **2**(4), 185–204 (1973). https://doi.org/10.1080/00423117308968441
4. Klomp, M., Thomson, R.: Influence of front/rear drive force distribution on the lateral grip and understeer of all-wheel drive vehicles. Int. J. Veh. Des. **56**(1–4), 34–48 (2011). https://doi.org/10.1504/IJVD.2011.043272
5. Horiuchi, S., Okada, K., Nohtomi, S.: Analysis of accelerating and braking stability using constrained bifurcation and continuation methods. Veh. Syst. Dyn. **46**, 585–597 (2008). https://doi.org/10.1080/00423110802007779
6. Abe, M.: A theoretical analysis on vehicle cornering behaviors in acceleration and in braking. Veh. Syst. Dyn. **15**(sup1), 1–14 (1986). https://doi.org/10.1080/00423118608969122
7. Bucchi, F., Frendo, F.: A new formulation of the understeer coefficient to relate yaw torque and vehicle handling. Veh. Syst. Dyn. **54**(6), 831–847 (2016). https://doi.org/10.1080/00423114.2016.1167225
8. Basilio Lenzo, A.S., Bucchi, F., Frendo, F.: On the handling performance of a vehicle with different front-to-rear wheel torque distributions. Veh. Syst. Dyn. **57**(11), 1685–1704 (2019). https://doi.org/10.1080/00423114.2018.1546013
9. Ono, E., Hosoe, S., Tuan, H.D., Doi, S.: Bifurcation in vehicle dynamics and robust front wheel steering control. IEEE Trans. Control Syst. Technol. **6**(3), 412–420 (1998). https://doi.org/10.1109/87.668041
10. Shuiwen Shen, P.S., Wang, J., Premier, G.: Nonlinear dynamics and stability analysis of vehicle plane motions. Veh. Syst. Dyn. **45**(1), 15–35 (2007). https://doi.org/10.1080/00423110600828285
11. Della Rossa, F., Mastinu, G., Piccardi, C.: Bifurcation analysis of an automobile model negotiating a curve. Veh. Syst. Dyn. **50**(10), 1539–1562 (2012). https://doi.org/10.1080/00423114.2012.679621
12. Pauwelussen, J.: Axle characteristics and vehicle limit cycle behaviour. Veh. Syst. Dyn. **0**(0), 1–19 (2024). https://doi.org/10.1080/00423114.2024.2322487
13. Farroni, F., Russo, M., Russo, R., Terzo, M., Timpone, F.: A combined use of phase plane and handling diagram method to study the influence of tyre and vehicle characteristics on stability. Veh. Syst. Dyn. **51**(8), 1265–1285 (2013). https://doi.org/10.1080/00423114.2013.797590
14. Wang, X., Li, W., Zhang, F., Li, Z., Bao, W.: Research on the vehicle steering and braking stability region. Appl. Sci. (2023). https://doi.org/10.3390/app13137806
15. Zhang, L., Ding, H., Guo, K., Zhang, J., Pan, W., Jiang, Z.: Cooperative chassis control system of electric vehicles for agility and stability improvements. IET Intel. Transp. Syst. **13**(1), 134–140 (2019). https://doi.org/10.1049/iet-its.2018.5079
16. Tremlett, A.J., Assadian, F., Purdy, D.J., Vaughan, N., A.P., M., Halley, M.: Quasi-steady-state linearisation of the racing vehicle acceleration envelope: a limited slip differential example. Veh. Syst. Dyn. **52**(11), 1416–1442 (2014). https://doi.org/10.1080/00423114.2014.943927
17. De Novellis, L., Sorniotti, A., Gruber, P.: Optimal wheel torque distribution for a four-wheel-drive fully electric vehicle. SAE Int. J. Passenger Cars Mech. Syst. **6**(1), 128–136 (2013). https://doi.org/10.4271/2013-01-0673
18. Pacejka, H.: Tire and Vehicle Dynamics. Elsevier (2005)
19. Kuznetsov, Y.A.: Elements of Applied Bifurcation Theory. Springer (1998)
20. Seydel, R.: Practical Bifurcation and Stability Analysis. Springer (2009)

21. Guckenheimer, J., Holmes, P.: Nonlinear Oscillations, Dynamical Systems, and Bifurcations of Vector Fields. Springer (1983)
22. Troger, H., Steindl, A.: Nonlinear Stability and Bifurcation Theory: An Introduction for Engineers and Applied Scientists. Springer (2012)
23. Hindiyeh, R.Y., Gerdes, J.C.: Equilibrium Analysis of Drifting Vehicles for Control Design. Dynamic Systems and Control Conference, vol. ASME 2009 Dynamic Systems and Control Conference, Volume 1, pp. 181–188 (2009). https://doi.org/10.1115/DSCC2009-2626
24. Edelmann, J., Plöchl, M.: Analysis of controllability of automobiles at steady-state cornering considering different drive concepts. In: Spiryagin, M., Gordon, T., Cole, C., McSweeney, T. (eds.) Dynamics of Vehicles on Roads and Tracks Vol 1, pp. 3–8. CRC Press, Rockhampton, Queensland, Australia (2017). https://doi.org/10.1201/9781351057264
25. Steindl, A., Edelmann, J., Plöchl, M.: Limit cycles at oversteer vehicle. Nonlinear Dyn. **99**(1), 313–321 (2020). https://doi.org/10.1007/s11071-019-05081-8
26. Steindl, A., Edelmann, J., Plöchl, M.: Hopf bifurcations for an oversteer vehicle—the influence of wheel load changes. PAMM (2021). https://doi.org/10.1002/pamm.202100179
27. Eberhart, M., Arndt, M., Edelmann, J., Plöchl, M.: Influence of the front-rear torque distribution on the handling characteristics and stability boundaries of an awd-vehicle. In: Mastinu, G., Braghin, F., Cheli, F., Corno, M., Savaresi, S.M. (eds.) 16th International Symposium on Advanced Vehicle Control, pp. 200–206. Springer, Cham (2024). https://doi.org/10.1007/978-3-031-70392-8_29
28. Milliken, W.F., Milliken, D.L.: Race car vehicle dynamics. SAE international Warrendale (1995)
29. Ploechl, M., Lugner, P., Edelmann, J.: Basics of longitudinal and lateral vehicle dynamics. In: Mastinu, G., Ploechl, M. (eds.) Road and Off-Road Vehicle System Dynamics Handbook, pp. 971–1021. CRC Press, Boca Raton (2014). https://doi.org/10.1201/b15560